Abstract submitted to: AFDAR International Workshop on
Advanced Flow Diagnostics for Aeronautical Research,
18-19 Feb. 2014, Lille, France

Application of Stereoscopic and Tomographic PIV in a Transonic Cascade

Joachim Klinner[1] and Chris Willert[1]

[1)] DLR Institute of Propulsion Technology, German Aerospace Center, 51170 Köln, Germany
Corresponding author: Joachim.klinner@dlr.de

Extended Abstract

Introduction

Tomographic PIV (tomo-PIV) and conventional stereo PIV (SPIV) are utilized in order to characterize the complex transonic flow within a highly loaded compressor cascade at Mach number $M_1 = 0.60$. In particular tomo-PIV has a high potential of recovering the unsteady, three dimensional corner flow on the suction sides of the cascade blades. The oil-streak image shown in **Fig. 1** [taken from Hergt et al., 2013] provides an impression of the complex transonic flow pattern at the intersection between end wall and the blade's suction side. The flow is dominated by a passage vortex which is driven by the pitch-wise pressure gradient between pressure and suction side. The time-averaged location of the vortex can also be predicted by a RANS (Reynolds averaged Navier Stokes) simulation as shown in **Fig. 2**. The vortex and the reverse pressure gradient along the cascade passage cause a flow separation between the end wall and the blade. In particular the high shear between the main passage flow and the passage vortex induces strong velocity fluctuations in a compressor cascade. Furthermore the corner separation leads to blockage effects which limit the mass flow capacity of the cascade. Under the given test conditions the simulations predict an extension of the passage vortex region of approximately $40\times24\times15$ mm^3.

The application of volume resolving thick-sheet PIV (or tomo-PIV) near the trailing edge of the cascade's blades is intended to demonstrate the technique's potential of instantaneously resolving secondary flow structures within the separation region of the cascade and its ability to derive three dimensional statistical data of fluctuations of velocity in the turbulent flow region.

Flow facility

The measurements are carried out in the transonic cascade wind tunnel (TGK) of the DLR Institute of Propulsion Technology. The TGK is a closed loop, continuously running facility with a symmetrical nozzle and a variable test section by adjustment of the lower end wall (**Fig. 3**). Additional suction capacities of the system allow the control of the side wall boundary layer in front of the cascade test section, in the upper and lower bypass channels as well as the transonic upper end wall. The suction capacities allow the adjustment of the static pressure across the channel height. Thereby, a homogeneous inflow according to an "infinite blade cascade" is achieved. The cascade consists of seven airfoils that are supported by transparent acrylic side walls of 16 mm thickness which provide suitable optical access for schlieren visualization as well as flow velocity methods such as laser-2-focus velocimetry (L2F) and particle image velocimetry (PIV).

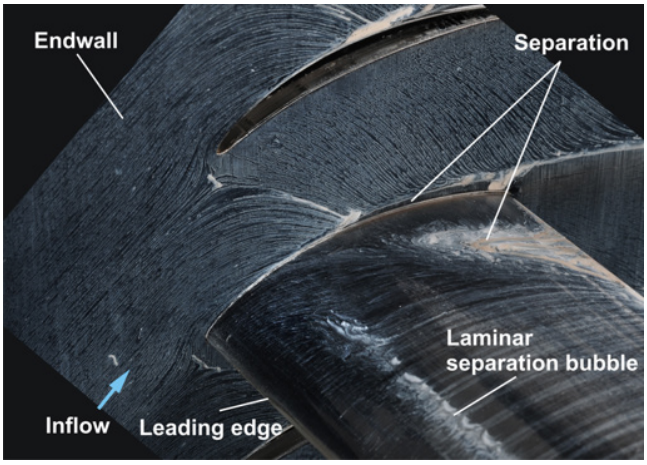

Fig. 1: Oil steak pattern of corner separation

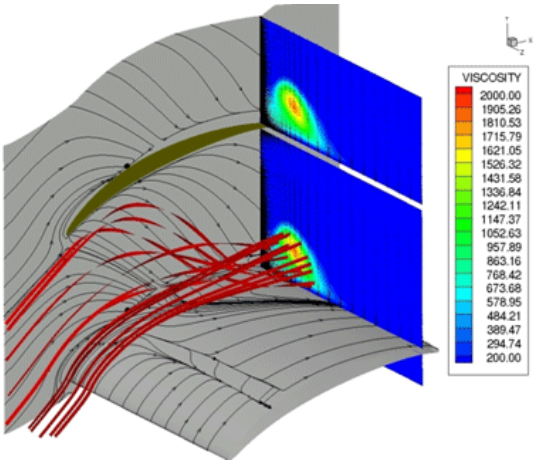

Fig. 2: RANS simulation of corner flow, the contour represents eddy viscosity

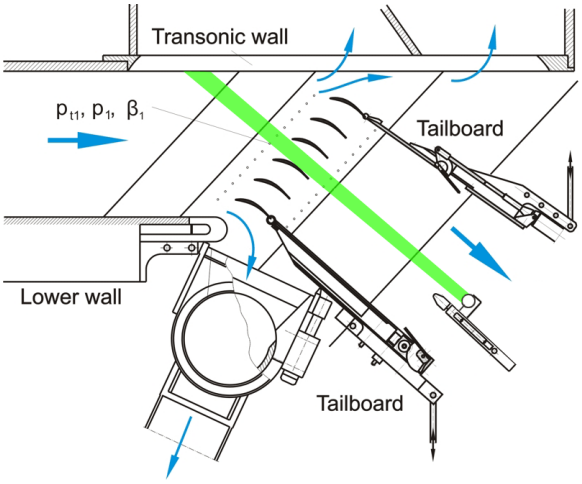

Fig. 3: The TGK test section and light-sheet orientation (green)

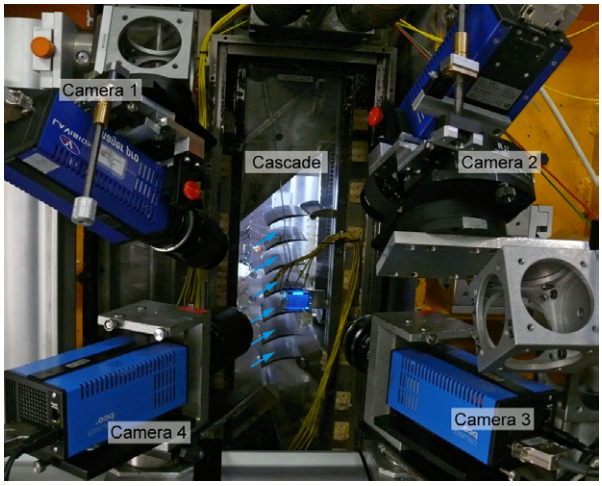

Fig. 4: Tomo PIV setup and back-illuminated calibration target on a micro traverse

Implementation of Volumetric PIV and Stereo PIV

Measurements are carried out near the suction side of a single passage in an area coincident with the numerically predicted location of the passage vortex. Fig. 3 shows a photograph of the tomographic PIV setup which involves four double-frame (PIV) cameras fitted with Scheimpflug mounts to account for the oblique imaging arrangement (**Fig. 4**). Two cameras observe the volume of interest along the suction side at zero pitch while the other camera pair observes the measurement volume from above at 26° and 34° pitch in order to have a sufficient angular aperture of the system.

Both single-axis and two-axis Scheimpflug mounts are used to optimize the depth of focus of each camera. The f-numbers range from 8...16 in order to minimize optical distortions due to the oblique viewing through the acrylic window. The observed common region of interest has a size of approximately 36×24 mm² and is located near the trailing edge of the blade. The thickness of the illuminated volume is successively adjusted to approximately 1 and 3.5 mm during each wind tunnel run. As highlighted in **Fig. 5**, image data is acquired in three regions at distances of 3, 8 and 11 mm from the side wall in order to cover the entire passage vortex. Each volume has a maximum size of 36×24×3.5 mm³ depending on the sheet thickness.

Within each region three additional thin sheet stereo PIV (SPIV) measurements are recorded and are later used for comparison (for details on SPIV see [Prasad, 2000, Raffel et al., 2007]).

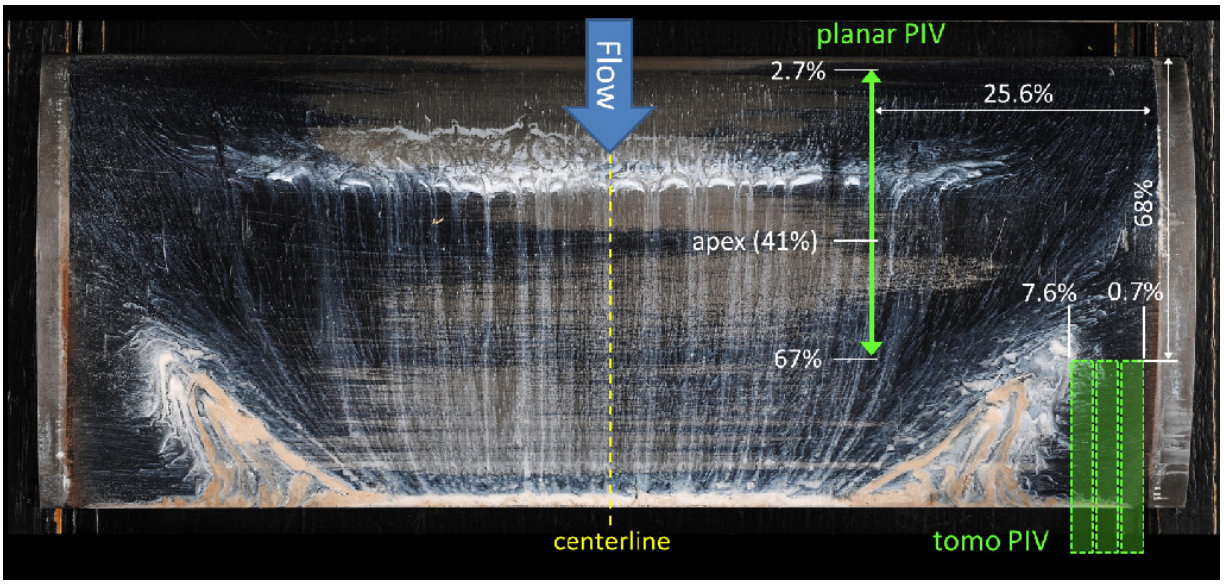

Fig. 5: Oil streak visualization of the suction side a single cascade blade overlaid with positions of PIV measurement areas. Vertical measures based on chord length, horizontal measures based on span width

Cameras no. 2 and no. 3 observe the illuminated volume with a backward scattering angle of -15° at effective f-numbers $f_{\#}14$ and $f_{\#}11$, respectively, in order to keep astigmatic distortion at an acceptable level. Therefore these cameras have the lowest sensitivity in the present imaging configuration. At maximum sheet thickness these cameras deliver a minimum net signal of about 150 signal counts per particle (after background intensity subtraction) which corresponds to only a few per cent of the camera's dynamic range (14 bit for camera models pco.1600 / pco.2000).

The cascade wind tunnel facility is seeded with an atomized paraffin-ethanol mixture (1:2) dispersed by two atomizers. An impactor and a dryer between atomizer and test section limited the maximum droplet diameter to approximately 1 µm. In an effort of improving the global seeding homogeneity a seeding injection rake was installed on the screens within the settling chamber upstream of the test section. This ensured the distribution of the particles over a larger area compared to streamline seeding. A response time evaluation of the applied seeding can be found in [Klinner et al., 2012, 2014] and reports a shock response time of 0.77±0.15 µs based upon based upon velocity profiles measured across a normal shock at M_1=1.25. The average response length corresponds to 0.23±0.045 mm. Based on Stokes drag law for spherical particles and a particle density of ρ_p=0.85 g/cm³ with the ethanol part fully evaporated and a maximum particle slip velocity of Δu=150 m/s this would lead to an average particle diameter of about d_p=0.4 µm. The achieved particle image density was evaluated using image segmentation algorithms based on connected component labelling. In the thick sheet configuration the measured particle image density in the separated corner flow ranges between 0.015-0.024 ppp depending on the view's magnification. The particle image size varies between 2 and 5 pixel, is partially elliptical and depends on the effective f-number and on residual astigmatism effects within each particular view.

The volume is calibrated using seven images of a z-traversed micro target [Klinner & Willert, 2012] which consists of back-illuminated calibration points with a spacing of 2 mm and a size of 0.4 mm. The lateral accuracy of point spacing is ±0.3 µm while the traverse is specified with positioning accuracy in z of ±2 µm. The measured point correspondences of world and camera coordinates are used to fit mapping functions according to world-to-image and image-

to-world projection. The residuals of the world-to-image projection range from 0.16 to 0.3 pixel depending on the mapping function and camera. The highest re-projection error arises for camera no. 2 which has the highest off-normal angle of 37°.

Global image shifts due to tunnel vibrations are monitored simultaneously with tomographic measurements. The particle image recordings additionally contain images of laser illuminated small reference marks on the Perspex sidewalls. These small marks were correlated with appropriate regions of the average image of the PIV recording and allow a posteriori correction of camera movements with respect to each other.

Particle volume reconstruction and displacement recovery

Three-dimensional reconstruction of the imaged particle volume is achieved with the maximum entropy reconstruction technique (MENT, [Minerbo, 1979]). Details of implementation of the algorithm and a validation based on synthetic data can be found in **A1**. MENT was chosen because it offers a number of advantages with respect to the more established methods such as MART [Elsinga et al., 2006] or MLOS-SMART [Atkinson & Soria, 2009]. Foremost MENT can significantly increase reconstruction speed [Bilsky et al., 2012] because the computational complexity is low and is limited to the calculation of products, sums and ratios of intensities, whereas SMART requires exponentiation and elaborate calculation of weighting factors. Bilsky et al. found MENT to converge after 1 to 3 iterations while MLOS-SMART requires on the order of 10 to 20 iterations to achieve similar convergence levels. A further acceleration of the first step of MENT can be obtained if the processing of rows of pseudo images h_j^{k+1} is parallel distributed on several cores. To give an example, 20 iterations of a MLOS-SMART reconstruction of two time-steps of a volume of 0.5 GVoxel based on four views of approx.1.8 MPixel can take in the order of 18 min on a 12-core Intel workstation at 2.66 GHz and 24 GB RAM. The processing of two time-steps of the same volume of MENT took in the order of 3 minutes on the same workstation.

State-of-the-art cross-correlation processing is used for particle displacement recovery in both planar and volume PIV. Both algorithms employ a resolution pyramid the starts at a rather coarse grid and stepwise increases resolution while continually updating a predictor field [Scarano, 2002; Raffel et al., 2007]. To increase processing speed, factor N image or volume down-sampling is applied by summing N^2 adjacent pixels or N^3 voxels, respectively. At a given resolution level integer-based sample offsetting is applied in a symmetric fashion using the estimate from the previous resolution step [Westerweel et al., 1997; Wereley et al., 2001]. Intermediate validation is based on normalized median filtering as proposed by Westerweel & Scarano (2005). Once the desired final spatial resolution is reached image or volume deformation based on third-order B-splines is applied at least twice to further improve the match between the images or volumes and thereby improving the displacement estimates. The processing codes for both particle reconstruction and displacement recovery are highly parallelized using OpenMP to achieve optimal data throughput.

Results

Stereo PIV measurement data is acquired from a thin light sheet setup using cameras no.1 and no.3 with a combined viewing angle of 50°.The image data was processed with PIVview 3.5 (PIVTEC GmbH, Germany) using the PIV processing parameters summarized in **Table 1**.

Fig. 6 shows the secondary flow velocities obtained by averaging $N = 510$ individual PIV recordings. In order to emphasize the chord-wise vortex evolvement, six orthogonal planes are extracted from nine stereo PIV planes. The color represents the v-w-magnitude while the vectors show the v and w components. Secondary flow velocities in-between the SPIV planes

are obtained by inverse distance interpolation. Due to interaction with the main flow the vortex is deformed and velocities in the vicinity of the end wall are clearly increased. The separation region on the blades suction side (see **Fig. 1**) causes an increase of secondary flow velocities near the blades suction side.

Fig. 7 shows time-averaged velocities at two neighboring thick sheet positions and boundaries of each reconstructed domain. Six secondary flow planes within the volume are plotted to show the vortex evolvement. The colored contour represents v-w-magnitude, that is, the in-plane velocity. Regions outside the common intersection of all cameras are blanked as well as regions which have light sheet intensity clearly below 50%. Within each plane only the in-plane components of every third vector are plotted to enhance the visibility of the secondary flow which otherwise would be lost in the presence of the strong out-of-plane component (mean flow). The passage vortex can clearly be identified. The v-w-magnitudes are comparable to stereo PIV results (**see Fig. 6,** right). The increased secondary flow velocities near the blades suction side can also be observed in stereo PIV results. The magnitudes in this region are lower due to strong background intensity near the blade surface observed by obliquely viewing cameras no.1 and no.2.

A more quantitative comparison of the velocity data recovered by the respective methods can be achieved by extracting coinciding velocity profiles from the data sets such as shown in Fig. 8. Comparisons of this types as well as further details on the implementation and potential of tomographic PIV for turbomachinary applications will be subject of the proposed workshop contribution.

Table 1: Evaluation parameters of stereo PIV and tomographic PIV

	Stereo PIV (thin sheet)	**Tomographic PIV (thick sheet)**
FOV	approx. 36 x 24 mm	
Sheet Thickness FWHM	1.1 mm	3.5 mm
Preprocessing	Subtraction of min. image Median 3x3 High pass Gauss. weight 7x7 Low pass fix. Gauss 3x3	Subtraction of min. image Subtr. of loc. minimum (kernel 5x5) normalization by avg. image clipping of intensities < thres.
Mapping algorithm	Projection map order 2 and disparity correction	Ratios of 2^{nd} order polynomials
Image Interpolation	B-Spline, degree 4	Bilinear, 4-neighboors
Reconstruction | Sampling	-	MENT, 2 iterations | ≈1 voxel /pixel
Interrogation method	Multigrid, 3 levels	3D Correlation, Multigrid, 3 levels
	Image deformation, 3 passes	Image deformation, 3 passes
Peak detection	Whittaker reconstruction	3x 3-point Gauss fit
Size of ROI | Mag.	1800x1200 px | 50 px/mm	1800x1200x300 vx | 50 vx/mm
Interrogation window size	64x48 px	64x32x32 vx
Sampling grid	32x24 px	32x16x16 vx
Final vector field	55x49	54x74x13
Vector validation	Maximum displacement diff. = 5 px Normalized Median thres.= 3	Normalized Median thres.= 3 sheet intensity > 50%

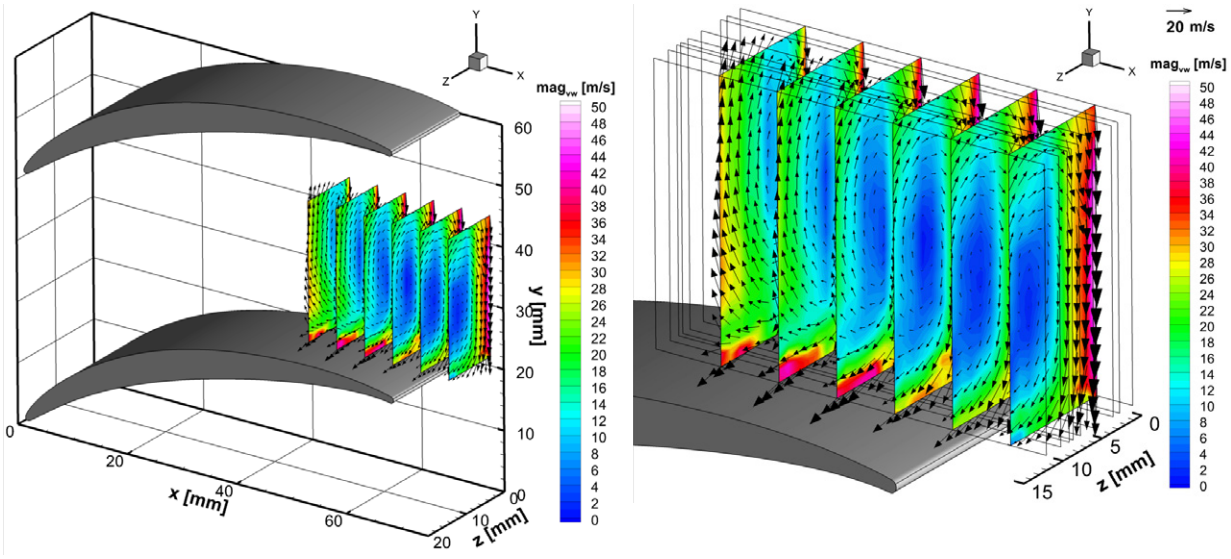

Fig. 6 Time averaged secondary flow velocities obtained from averaged SPIV measurements at 9 planes each with 1mm sheet thickness; overview (left) and detailed flow field and boundaries of the SPIV planes (right)

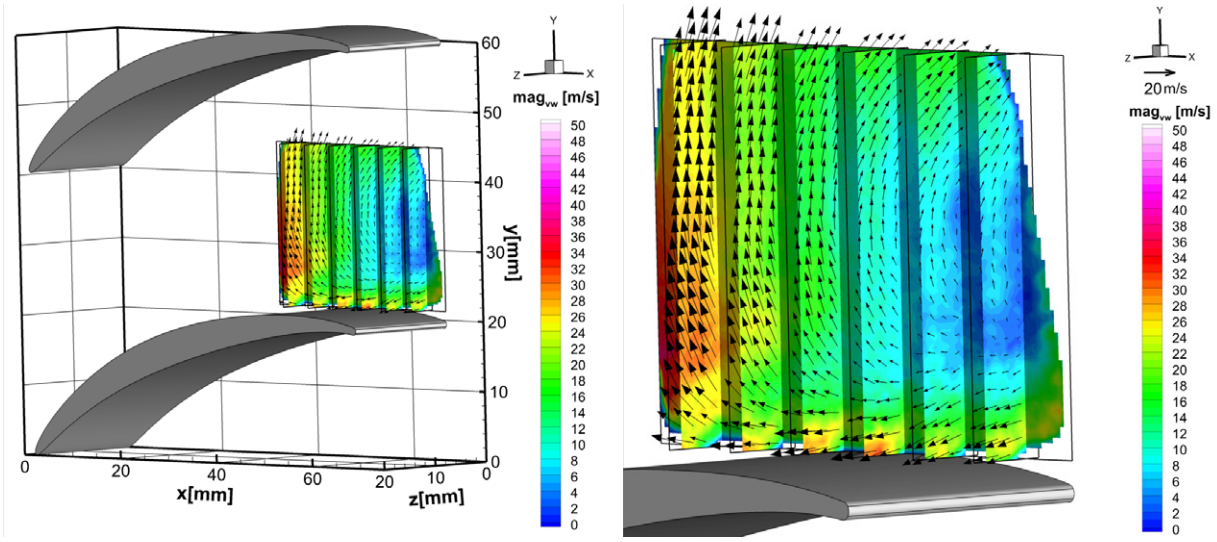

Fig. 7: Average of N=100 tomographic measurements for a volume of 36×24×4 mm³ at z=11 mm distance to the end wall; overview (left) and detailed flow field with boundaries of reconstructed domain (right). Only every third vector along each dimension is plotted

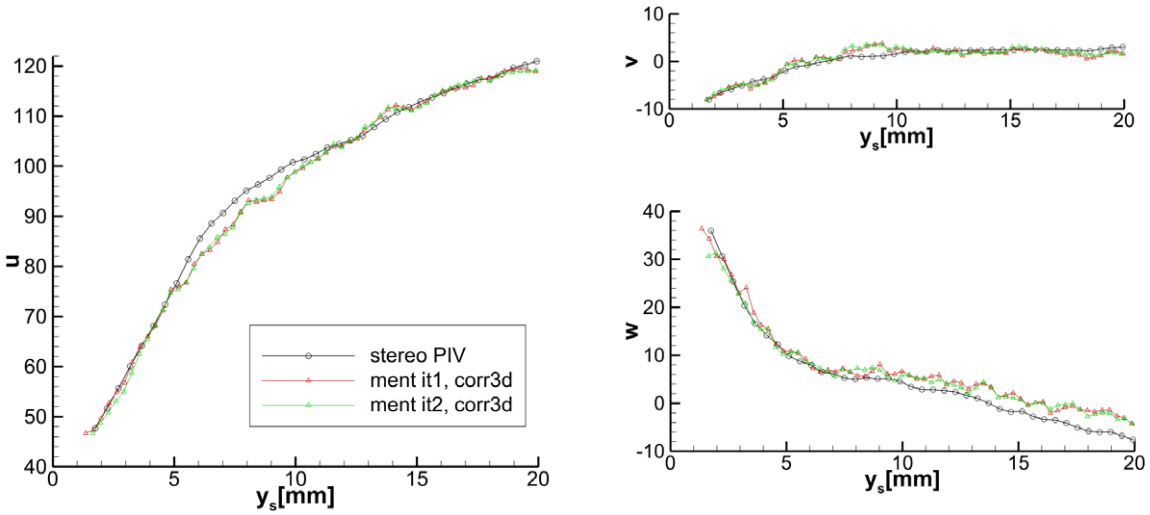

Fig. 8: Comparison of velocity profiles extracted at x=60 mm for stereo PIV and tomo-PIV

References

Atkinson C, Soria J (2009) An efficient simultaneous reconstruction technique for tomographic particle image velocimetry, *Exp. Fluids* **47**:563-578

Bilsky AV, Markovich DM, Tokarev MP, Lozhkin VA (2012) Low computation cost reconstruction technique for tomo-PIV; *Proceedings: 16th Intl. Symp. on Applications of Laser Techniques to Fluid Mechanics, Lisbon, July*

Elsinga GE, Scarano F, Wieneke B, van Oudheusden BW (2006) Tomographic particle image velocimetry, *Exp. Fluids* **41**(6):933-947, doi 10.1007/s00348-006-0212-z

Hergt A, Steinert W, Grund S (2013) Design and Experimental Investigation of a Compressor Cascade for Low Reynolds Number Conditions, *Proceedings: 21th International Symposium on Air Breathing Engines, ISABE-2013-1104*, Busan, South Korea, 09-13 Sept.

Klinner J, Hergt A, Beversdorff M, Willert C (2012) Visualization and piv measurements of the transonic flow around the leading edge of an eroded fan airfoil; *Proceedings: 16th Intl. Symp. on Applications of Laser Techniques to Fluid Mechanics, Lisbon, July*

Klinner J, Willert C (2012) Tomographic shadowgraphy for three-dimensional reconstruction of instantaneous spray distributions; *Exp. Fluids* **53**:531-543

Minerbo G (1979) MENT: A maximum entropy algorithm for reconstructing a source from projection data. *Graphics and Image Processing* **10**, 1979

Prasad AK (2000): Stereoscopic particle image velocimetry. *Exp. Fluids* **29**(2): 103-116, doi 10.1007/s003480000143

Raffel M, Willert C, Wereley S, Kompenhans J (2007): "Particle Image Velocimetry, A Practical Guide". Springer Berlin-Heidelberg, ISBN 978-3540723073

Scarano F (2002) Iterative image deformation methods in PIV. *Meas. Sci. Technol.* **13**(1), R1

Schanz D, Gesemann S, Schroeder A, Wieneke B, Novara M (2012) Non-uniform optical transfer functions in particle imaging: calibration and application to tomographic reconstruction, *Meas. Sci. Technol.* (Submitted)

Wereley ST, Meinhart, CD (2001) Second-order accurate particle image velocimetry. *Exp. Fluids* **31**(3):258–268

Westerweel J, Dabiri D, Gharib M (1997) The effect of a discrete window offset on the accuracy of cross-correlation analysis of digital piv recordings. *Exp. Fluids* **23**(1):20-28

Westerweel J, Scarano F (2005) Universal outlier detection for PIV data. *Exp. Fluids* **39**(6):1096–1100

Wieneke B. (2007) Volume self-calibration for stereo PIV and tomographic PIV, *Exp. Fluids* **45**:549-556